Editors' Suggestion

Identification of nonradiative recombination channels in $Ga_{0.2}Al_{0.8}N$-AlN wells with deep ultraviolet emission at 215 nm

Alexandra Ibanez,[1] Sunanda Mitra,[2] Sylvia Hagedorn,[3] Wilfried Desrat,[1] Pierre Valvin,[1] Guillaume Cassabois,[1,4] Julien Brault,[2] and Bernard Gil[1,*]

[1]*Laboratoire Charles Coulomb, CNRS, Université de Montpellier, F-34095 Montpellier, France*
[2]*Université Côte d'Azur, CNRS, CRHEA, rue Bernard Grégory, 06905 Sophia Antipolis, France*
[3]*Ferdinand-Braun-Institut (FBH), Gustav-Kirchhoff-Straße 4, 12489 Berlin, Germany*
[4]*Institut Universitaire de France, 75231 Paris, France*

(Received 31 May 2026; accepted 29 September 2026; published 9 November 2026)

The optical efficiency of deep-ultraviolet nitride-based heterostructures emitting at wavelengths around 215 nm remains severely limited by thermally activated nonradiative recombination processes. In this article, we investigate the optical properties of high-quality $Ga_{0.2}Al_{0.8}N$ multiple quantum wells grown by molecular beam epitaxy on AlN templates fabricated either by metal-organic chemical vapor deposition or by molecular beam epitaxy. The temperature-dependent photoluminescence measurements performed in the 10–300 K range reveal that the thermal quenching of the photoluminescence emission is governed by three distinct activation processes common to all the sample series. The first nonradiative recombination channel, characterized by an activation energy in the 4–8 meV range, is extrinsic in origin and is associated with impurities as well as with the density of structural defects within the crystal. The second process, with an activation energy of 70 meV, is intrinsic in nature and is related to the thermal dissociation of the free exciton. A third thermally activated process, also intrinsic, exhibits an activation energy of approximately 130 meV and is assigned to the thermal escape of electrons and/or holes from the active region of the multiple quantum wells, leading to a further reduction in optical efficiency at elevated temperatures.

DOI: 10.1103/3yzl-jn7v

I. INTRODUCTION

The field of light emitting devices operating in the deep ultraviolet (DUV) range, particularly the light-emitting diodes (LEDs) relying on spontaneous emission at wavelengths between 200 and 280 nm, is currently experiencing a rapid global development. The objective is to design and manufacture high-performance components capable of fulfilling key roles, such as replacing mercury vapor lamps in order to comply with the Kyoto Protocol [1], while also addressing a wide range of environmental, biological, and medical applications [2–10]. Although intense emission at 215 nm has recently been demonstrated via photoexcitation of fluorescence using twisted boron nitride layers [11], and this is a very noticeable result [12], wurtzite-structured nitrides of the (In, Al, Ga)N family remain, at present, the only viable candidates for the industrial production

*Contact author: bernard.gil@umontpellier.fr

Published by the American Physical Society under the terms of the Creative Commons Attribution 4.0 International license. Further distribution of this work must maintain attribution to the author(s) and the published article's title, journal citation, and DOI.

of such advanced devices down to approximately 210 nm [13]. This area of research has progressed swiftly through the use of $Ga_{1-x}Al_xN$-AlN heterostructures, building upon decades of prior studies on the $Ga_{-y}In_yN$-$Ga_{1-x}Al_xN$ system, which has amply demonstrated its potential for the fabrication of diodes operating across the short-wavelength visible spectrum from red to ultraviolet B [14]. However, these rapid advances are hindered by a sharp decline in the external quantum efficiency of ultraviolet C devices when the emission wavelength falls below 260 nm [15].

Several physical phenomena inherent to the $Ga_{1-x}Al_xN$ alloy used to form quantum wells (QWs) embedded within AlN barriers limit the performance of these devices at shorter wavelengths:

(1) The lack of shallow impurity for realizing *p*-doped $Ga_{1-x}Al_xN$. Despite investigations regarding Zn, Be, and Ca, only Mg has been found to be the *ad hoc p*-type dopant after thermal posttreatment for its passivation from hydrogen. The binding energy of Mg in $Ga_{1-x}Al_xN$, and its activation rate are critical factors that influence the efficiency of *p*-type doping. The activation energy of Mg decreases from about 500 meV in AlN [16] to approximately 160–200 meV in GaN [17]. For Mg in GaN, the activation rate, that is to say, the fraction of dopants that are actually activated and contribute to conduction, is about less than or on the order of 10% in doped samples, due to defect compensation and hole trapping [17]. This means that a large portion of the incorporated Mg remains inactive. The activation rate of Mg in AlN is thus even lower than it is for GaN, making efficient electrical injection through Al-rich heterostructures very difficult. Of course, incorporation of Mg is limited physically and also for the propensity to form compensating structural defects beyond a critical density of Mg atoms, a very general trend in wide-bandgap semiconductors [18].

(2) For $Ga_{1-x}Al_xN$ grown in the (0001) plane with lattice matching to AlN, a change in valence band symmetry at around $x \approx 0.7$ compared to $x \approx 0.1$ in the bulk [19], which prevents efficient light extraction at high aluminum content due to a crossover from transverse electric (TE) to optically forbidden transverse magnetic (TM) emission [20–23].

(3) The presence of intrinsic electric fields in heterostructures grown along the ⟨001⟩ direction, which is the preferred orientation of wurtzite crystals when growing them on low-cost (0001) sapphire substrates [24–29]. It is required to manage it and to reduce it as much as possible, in particular, by using thin-layer QWs, tuning the barrier width [30], and many other approaches, including technological processing recipes that are out of our scope here. These phenomena are now decently understood. Alternatively, potentially promising approaches to achieving higher internal quantum efficiency (IQE) and arm twisting the consequences of the switch from TE to TM light emission earlier alluded to may be the use of sapphire substrates with M-, A-, or R-plane orientations, enabling growth along nonpolar or semipolar directions [31].

(4) The lattice mismatch between the sapphire substrate and the various nitride layers of the active part of the device that generate a lot of structural defects acting as nonradiative carrier recombination channels. Homoepitaxial growth on bulk AlN substrates, the material to be used for the barriers enclosing the thin QWs, could be an option in case of devices operating at the shortest possible wavelengths. This is of course an expensive option but, for conditions when reducing the emission wavelength is so challenging, it could become an ultimate solution having in mind the fact that bulk AlN can be *a priori* prepared in terms of epi-appropriate surfaces with any reticular plane orientation.

II. EXPERIMENTAL METHODS

A lot of studies on DUV light-emitting heterostructures remain limited to devices grown under standard ⟨001⟩ conditions and to the exploration of solutions for enhancing their performances. It is noticeable that studying the evolution of their performances from the low-temperature regime relevant to solid-state physics predictions to the operational temperatures of practical optoelectronic devices has remained almost confidential. The present work addresses such an investigation through this broad temperature range. We report here on a comparative study of the relative performances of $Ga_{0.2}Al_{0.8}N$-AlN multiple quantum well (MQW) heterostructures, consisting of four wells with

TABLE I. Description of the structural and optical parameters of the samples (SNG, STD, and HTA): full-width-at-half-maximum values of the AlN pseudosubstrates rocking curve (002) and (101) peaks (columns 2 and 3); estimated dislocation densities from XRD measurements (column 4); values of the parameters A_i (with $A_i = \frac{\Gamma_i}{\gamma_{\text{rad}}}$) related to the nonradiative recombination channels (columns 5–7); and activation temperatures of the three nonradiative channels (columns 8–10).

Sample	Rocking curve (002) (deg)	Rocking curve (101) (deg)	Dislocation density (cm^{-2})	A_1	A_2	A_3	T_1 (K meV)	T_2 (K meV)	T_3 (K meV)
SNG	0.017	0.100	8.1×10^8	17	10^4	1.2×10^6	80-7	800-70	1500-130
STD	0.307	0.667	3.9×10^{10}	300	10^5	9×10^6	60-5	800-70	1500-130
HTA	0.070	0.139	1.7×10^9	450	10^5	5×10^6	45-4	800-70	1500-130

nominal thicknesses of 2 nm separated by 4-nm-thick AlN barriers. These MQWs have been designed for emitting light at ∼215 nm, and they were deposited at around 850 °C and at a growth rate of 75 nm/h by molecular beam epitaxy (MBE) on three different AlN pseudosubstrates, as described below, deposited on (001)-oriented sapphire:

(1) An AlN pseudosubstrate supplied commercially by Sino-gan [32] and grown by metal-organic chemical vapor deposition (MOCVD). The AlN thickness used is 2.1 μm (as specified by Sino-gan). We controlled this specification experimentally by optical interference measurement. This sample is denoted as "SNG" hereafter.

(2) An AlN pseudosubstrate grown at Centre de Recherche sur l'Hétéro-Epitaxie et ses Applications (CRHEA) by MBE using the conditions described in Ref. [33]. The thickness of the sample studied here is 0.2 μm and we denote it as "STD" hereafter.

(3) An AlN pseudosubstrate grown at CRHEA by MBE, which experienced a complementary postgrowth high-temperature annealing treatment in a furnace in N_2 atmosphere at 1700 °C, following the conditions described in Ref. [34], in order to improve its crystalline quality. We denote it as "HTA" hereafter.

X-ray diffraction (XRD) experiments permit the evaluation of the densities of dislocations (mixed+edge) at the surface of the pseudosubstrates from the full width at half maximum (FWHM) of the rocking curves for the symmetrical (002) and asymmetrical (101) diffraction peaks [35]. This is reported in Table I, columns 2–4. The table indicates a reduction of the dislocation densities when MBE-grown pseudosubstrates undergo a postgrowth high-temperature annealing treatment. It is also important to note that the in-plane lattice constant for the HTA MBE-grown template is decreased by the high-temperature annealing process. The as-grown AlN MBE layer (labeled as STD) is compressively stressed, with a value of around 0.07%, while the HTA AlN MBE layer is compressively stressed, with a value of around 0.31%.

Our photoluminescence (PL) setup for PL spectroscopy in the DUV has been previously described [22,23,33]. The samples were excited using the fourth harmonic of a Ti:sapphire laser ($\lambda = 196$ nm) with an average power of 50 μW focused onto a spot of approximately 50 μm in diameter. With 80 MHz repetition rate, this corresponds to approximately 6×10^5 photons per pulse, i.e., a carrier sheet density on the order of 3×10^{10} cm^{-2} per pulse (or approximately 10^{16} cm^{-3} in the MQW active region assuming complete absorption). Considering the limited absorption in the active region, the actual carrier density is expected to be even lower, ensuring that the measurements were performed in the low-injection regime.

A power-dependent PL study would have been of interest. However, reducing the excitation power even by one order of magnitude leads to a drastic degradation of the signal-to-noise ratio. Under these conditions, the PL signal becomes too weak to be reliably detected over the full temperature range up to 300 K, making such measurements impractical with the present samples.

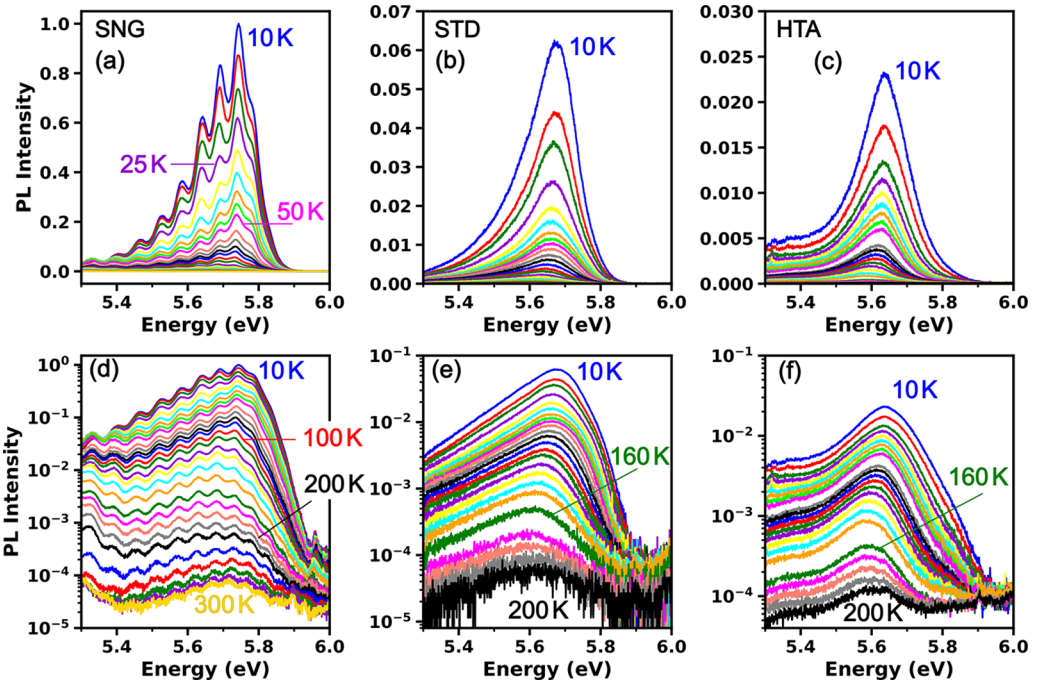


FIG. 1. The triptych representation scaling from panels (a) to (c) represents the evolution of the PL features in a linear *y* scale. The PL intensities are all plotted as a function of the PL intensity of SNG measured at 10 K, taken as a reference value. The triptych representation scaling from panels (d) to (f) represents the evolution of the PL features in a logarithmic *y* scale to allow the visualization of the fluorescence at room temperature and to indicate that the data analysis is still possible at 300 K.

III. EXPERIMENTAL RESULTS

In this study, we find that the variation of the IQE is ruled by three different nonradiative recombination channels, with activation energies of ∼4−7, ∼70, and ∼130 meV, respectively. The low-temperature activation energy is of extrinsic origin, correlated to the density of dislocations (DD) in the different pseudo-substrates. The DDs were deduced from the x-ray diffraction analysis of the full width at half maximum of the (002) and (101) diffraction peaks (Table I) [35]. The other two activation energies are of intrinsic nature and of paramount interest: They, respectively, correspond to the thermal dissociation of the exciton (whose binding energy at 77 meV was computed using a variational calculation of the electron-hole long-range Coulomb interaction) and to the thermal escape of the Γ_7 hole out of the confining $Ga_{0.2}Al_{0.8}N$ QW layers (obtained from a $\mathbf{k}\cdot\mathbf{p}$ effective mass calculation).

In Figs. 1(a)–1(c) are linearly plotted the evolutions of the PL intensities between temperatures $T = 10$ K and $T = 300$ K. The PL intensity recorded for sample SNG at 10 K is stronger than what we previously measured at this wavelength for other MQW samples with similar designs [36]. Note the weaker emission for the MBE-grown samples as indicated along the *y* axes of the plots, which prevent to propose consolidated values of the PL intensities at temperatures above 200 K in the chosen range of photoexcitation densities. The undulations observed in case of the SNG MOCVD-grown sample are interference fringes in the thick AlN pseudosubstrate. They are not so readily observed for samples grown on thinner MBE-grown pseudosubstrates, interference fringes being about one order of magnitude larger in the latter than in the former. The PL features peak at ∼215 nm for all samples at 10 K. They all exhibit low-energy PL wings as evidence of unresolved contributions of alloy disorder and broad phonon replicas [23]. Fitting the high-energy wings by a

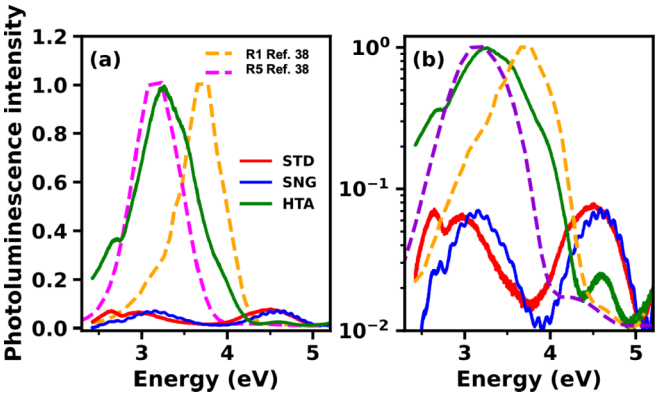


FIG. 2. Photoluminescence spectra measured at 10 K for the $Ga_{0.2}Al_{0.8}N$-AlN MQW heterostructures grown on different AlN pseudosubstrates. (a) Linear scale. (b) Logarithmic scale. The spectra of the SNG and STD samples are normalized to the near-band-edge emission at 5.5 eV, whereas the HTA spectrum and the cathodoluminescence spectra reported by Chichibu *et al.* [38] for samples R1 (unintentionally doped AlN) and R5 (heavily Si-doped AlN) are normalized within the 3–4 eV spectral region (dashed lines).

Gaussian, we deduce FWHM values of 118, 134, and 188 meV for the zero-phonon lines for the SNG, STD, and HTA samples, respectively, which indicates moderate different crystalline qualities through the series of samples. Note that, at a nominal composition of 80% Al, a fluctuation of 1% in the Al composition shifts the bandgap energy of the strained-layer alloy by an amount of $\sim\pm25$ meV around the average value of 5.6 eV, which indicates that the distribution of energies, i.e., associated with the PL peak FWHMs, is in the acceptable experimental limit. In addition, fluctuations of the thickness of the quantum wells can be expected, which is an experimental uncertainty. The intensities of emission bands at 5.6 eV are in ratio of 1, 0.3, and 0.16 at 10 K for the SNG, STD, and HTA samples, respectively. In Figs. 1(d)–1(f) are plotted the same PL spectra on a logarithmic scale.

It is worth noting that the pseudosubstrates exhibit two broad PL bands extending from approximately 3 to 5 eV at 10 K, as shown in Figs. 2(a) and 2(b). These emissions are by more than one decade weaker than the emissions at 5.6 eV and we remind that the intensities of emission bands at 5.6 eV are in ratio of 1, 0.3, and 0.16 at 10 K for the SNG, STD, and HTA samples, respectively. In the SNG and STD samples, the emissions centered around 3.2 and 4.5 eV display comparable intensities. In contrast, the HTA sample exhibits a pronounced enhancement of the 3.2-eV-related band whose intensity exceeds that of the 4.5 eV emission by approximately a factor of 40. This may be attributed to diffusion in the AlN of oxygen and complexes involving vacancies [37–39] during the annealing. The strong predominance of the 3.2 eV emission in the HTA sample may suggest that the high-temperature annealing treatment promotes a thermally activated redistribution of vacancy-related defects, possibly involving nitrogen-vacancy complexes and oxygen-related aluminum-vacancy centers formed during annealing at 1500 °C in the thin MBE-grown AlN pseudosubstrate. To progress toward the identification of the defect-related luminescence features, we compare the PL of our samples with the cathodoluminescence spectra reported by Chichibu *et al.* [38] for samples they labeled as R1 and R5. We have made a digitization of the former followed by a further normalization to the PL intensity of the HTA sample within the 3–4 eV spectral region. Under this representation, the spectral shape of the HTA sample closely resembles the defect-related luminescence bands reported by Chichibu *et al.* [38] in Si-doped AlN layers. In particular, the broad emissions observed in the 3.2–3.5 eV range have been attributed to $V_{Al}(O_N)_n$ complexes, whereas the weaker PL band in the 4.5 eV has been associated with $Si_{Al}-C_N$ nearest-neighbor defect complex [39].

In Figs. 3(a)–3(c) are represented logarithmically, using colored dots, the evolutions of the PL intensities as a function of the temperature. This representation is required to precisely and readily

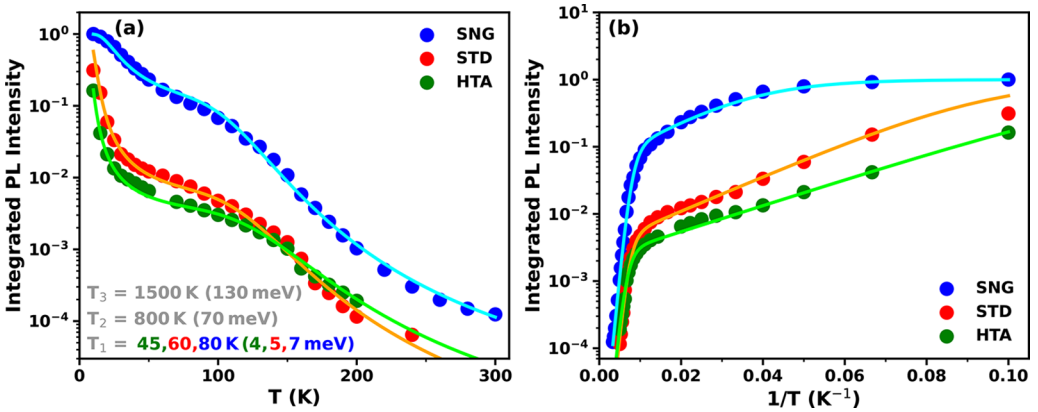


FIG. 3. Plots of the integrated PL intensity for the three samples: SNG (blue), STD (red), and HTA (green). The symbols represent the experimental data, while the solid lines correspond to the fits. The T_i values denote the activation temperatures, with the corresponding activation energies given in parentheses: (a) as a function of temperature and (b) as a function of the inverse temperature.

evidence the intensity variations related to the different nonradiative recombination channels that rule the PL intensity with temperature. The intensity of the SNG sample was arbitrarily set to unity at 10 K and taken as a reference value. Consequently, the intensities of the PL peaks for the two other samples were plotted relative to it.

IV. DATA INTERPRETATION

The variation of the internal quantum efficiency is proportional to

$$\mathrm{IQE}(T) \propto \frac{\gamma_{\mathrm{rad}}(T)}{\gamma_{\mathrm{rad}}(T) + \gamma_{\mathrm{nr}}(T)}, \tag{1}$$

where $\gamma_{\mathrm{rad}}(T)$ is the radiative recombination rate and $\gamma_{\mathrm{nr}}(T)$ represents the nonradiative recombination rate. It is found that $\gamma_{\mathrm{nr}}(T)$ is ruled by three different temperature-activated nonradiative channels, which need to be considered for fitting the data. The nonradiative recombination rate is written as

$$\gamma_{\mathrm{nr}}(T) = \sum_{i=1}^{i=3} \Gamma_i e^{\frac{-T_i}{T}}, \tag{2}$$

where Γ_i is the prefactor associated with the ith thermally activated nonradiative recombination channel. Keeping in mind that localization effects substantially rule the FWHM of PL lines for heterostructures in this range of composition [23], we treat $\gamma_{\mathrm{rad}}(T)$ as a constant from 10 to 300 K [40–42]. We know from the recent works of Dr. Aurélien David, who published a review article in June on InGaN-based LEDs [41] and more recently in July [42], that the localization of charge carriers is only partial. Facing the difficulties for a robust modeling of $\gamma_{\mathrm{rad}}(T)$ and its probable spectral dependence, we have therefore chosen to be cautious in our analysis, and for limiting the number of fitting parameters, we took the simplest approximation that does not impact significantly the physics of the temperature dependence of the light emission in these samples. Fitting the PL intensity indicates that the different non-radiative recombination channels are ruled by activation energies $k_{\mathrm{B}}T_i$ of ∼4−7, ∼70, and ∼130 meV, respectively, through the series of samples, where k_{B} is the Boltzmann constant. The activation energies of ∼70 and ∼130 meV are common to all samples and the ratios of nonradiative to radiative recombination, $A_i = \frac{\Gamma_i}{\gamma_{\mathrm{rad}}}$, increase with decreasing AlN crystalline quality. We emphasize that the same values for T_2 and T_3 appear

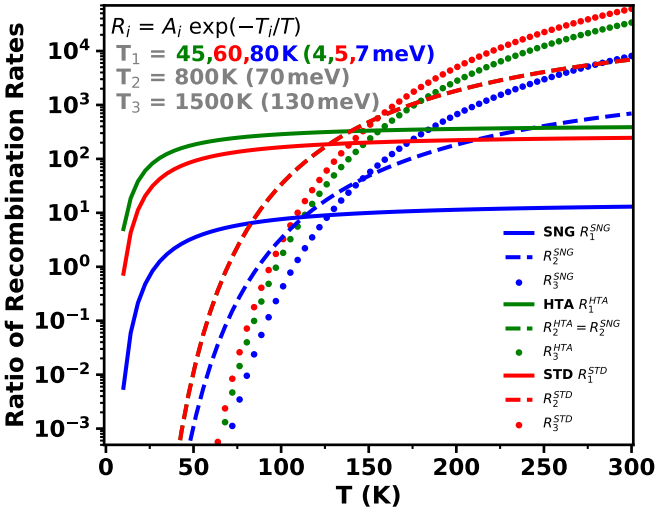


FIG. 4. Plot of the three nonradiative recombination regimes for the SNG (blue), STD (red), and HTA (green) samples (see text for details).

naturally without any constraint. The full set of numbers determined from the fitting procedure is available in Table I, in columns 8–10. It is worth noting that the rate of nonradiative recombination is the lowest for sample SNG and the highest for sample HTA. This result is in line with the intensity of the broad bands that act as efficient traps for photocreated electron and hole pairs. The enhanced crystalline coherence for sample HTA compared to sample STD has an impact on the PL properties: At high temperature, the PL of sample HTA is the most robust, with parameter A_3 for HTA being smaller than that for STD. Globally, the nonradiative recombination rate decreases with improved "overall quality" of the pseudosubstrate.

In Fig. 4, we plot the different nonradiative recombination channels deduced from the fitting of the PL intensities as a function of T. The color code associated with the three samples in Figs. 3(a)–3(c) has been kept for clarity. The low-temperature recombination channels are represented using full lines, the 800 K activated decays are plotted using dashed lines, and plots with dots correspond to the high-temperature (1500 K) efficient nonradiative recombination channels. It is clearly seen in the figure that the low-temperature effect is clearly related to the density of dislocations in the pseudosubstrates and also pleads in favor of an impact of its thickness (i.e., around 2 μm for SNG sample compared to several hundreds of nanometers for STD and HTA samples). We have compared the efficiency of the PL emission for SNG with the PL emission of a previous series of MQW samples grown by MBE on the MOCVD-grown thinner pseudosubstrate (see Ref. [36]). Although the MQW samples have slightly different designs, they are fully comparable in terms of the FWHM of their PL peak emission. At this stage, it was found that sample SNG is more robust with temperature. Indeed, its superior temperature robustness enables to evidence the third nonradiative recombination channel, which was not possible in previous studies [36]. Therefore, and from *bona fide*, the MBE growth protocol of the MQW active region is found to play a minimal role in the PL efficiency; this is rather the quality of the AlN template that plays a critical role. This paves the way for further detailed study of the effect of thickness and annealing of AlN templates grown by MBE for comparing with the MOCVD-grown commercial substrate.

In the following, some physical mechanisms related to the origin of the two nonradiative recombination channels efficient in the high-temperature range are discussed. In Fig. 5(a) are reported the evolutions of the potential depths for the electrons (green), spin-orbit split-off holes (blue), and heavy holes (red) for $Ga_{1-x}Al_xN$ QWs lattice matched to AlN. The light-hole to heavy-hole splitting is about 7–8 meV through the whole series of compositions (about twice the value of the Δ_2

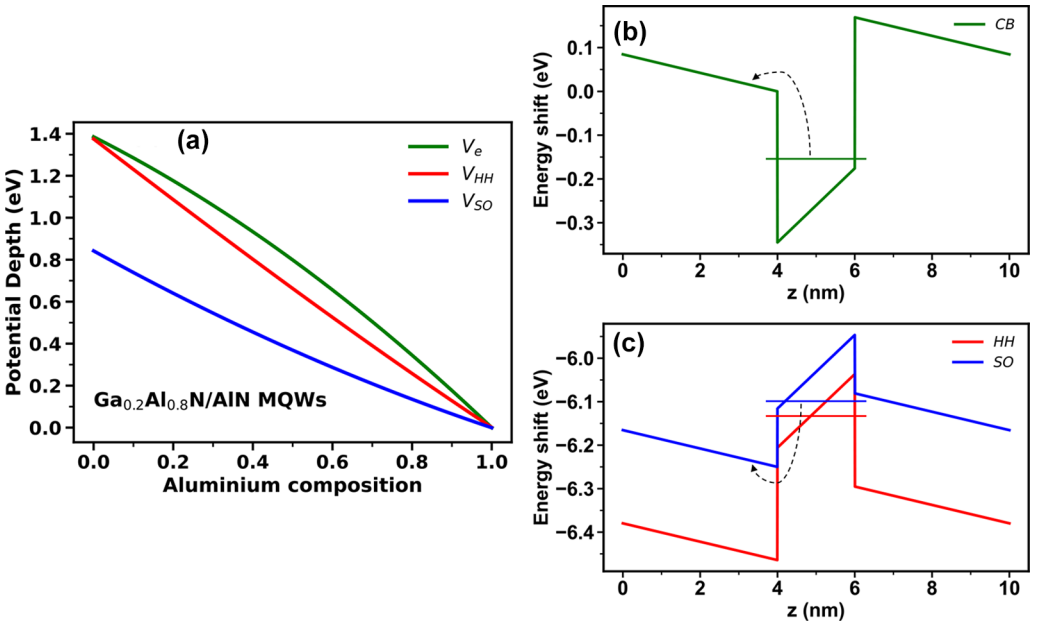


FIG. 5. (a) Values of the potential depths we used to calculate the confined levels for $Ga_{1-x}Al_xN$-AlN strained-layer quantum wells lattice matched to AlN. (b), (c) Band lineups for the conduction band (green), for the Γ_7 Bloch state corresponding to the spin-orbit split-off hole (blue), and for the Γ_9 heavy-hole Bloch state (red). The positions of the confined levels are indicated using the same color code.

spin-orbit coupling parameters); therefore, we restricted the figure to the position of the spin-orbit split-off and heavy-hole valence bands for the sake of its clarity. Then, we calculate the confined electron, spin-orbit split-off, and heavy-hole confined states. In Figs. 5(b) and 5(c), we represented the potential lineups for the conduction, spin-orbit split-off, and heavy-hole valence bands (green, blue, and red lines, respectively) together with the positions of the confined levels. The electric field in the QWs is estimated as 5 MV/cm at $x = 0$ and, thus, gives a 169 meV drop through the QW layer. The depth of the conduction band potential is 345 meV and the confinement energy is 191 meV at 154 meV from the top of the conduction band lineups. The value obtained by such a simple calculation is indicative that, in these samples, electron tunneling out of the quantum well layer as qualitatively indicated by the dashed arrow into AlN may be *a priori* good candidate for the third nonradiative recombination channel with a 130 meV activation energy.

Switching now to the split-off valence band, the potential depth is 135 meV and the confinement energy is 152 meV. As shown in Fig. 5(c), from the position of the level in blue relative to the band lineup, the right-hand part of the envelope function of the Γ_7 spin-orbit split-off hole (almost fully p_z-like) substantially tunnels in the AlN barrier layers. We believe that such calculation is also indicative that, in these samples, thermal-induced tunneling of the spin-orbit split-off hole out of the quantum well layer as qualitatively indicated by the dashed black arrow into AlN may also be *a priori* good candidate for the third nonradiative recombination channel with a 130 meV activation energy. The hole mass is very anisotropic in nitrides and its value for the spin-orbit split-off hole used for the $\mathbf{k}\cdot\mathbf{p}$ calculations is comparable to the effective mass of the electron mass. The knowledge of many parameters of the effective mass calculation, including the distribution of the gap mismatch between the strained-layer quantum well and AlN into conduction and valence bands (the band offset ratio), is moderate, so we are left to conclude that both the electron and the spin-orbit split-off hole contribute jointly to the third nonradiative recombination channel, although their respective contributions cannot be distinguished. Regarding the heavy hole, the Γ_9 Bloch state

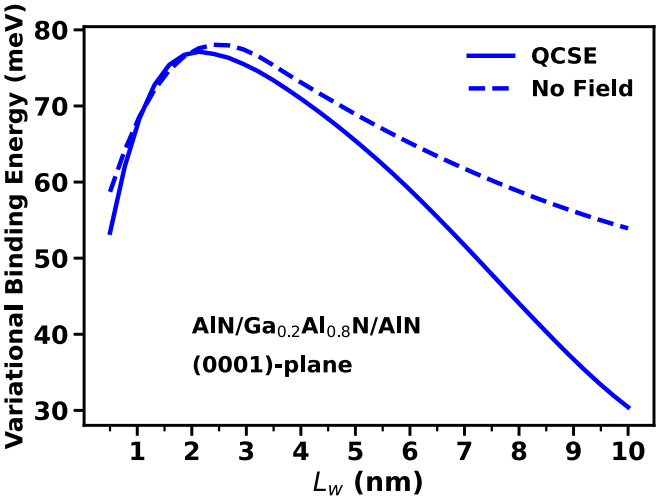


FIG. 6. Computed exciton binding energies in strained-layer $Ga_{0.2}Al_{0.8}N$-AlN quantum wells lattice matched to AlN. The full line includes the QCSE, whereas the dashed line indicates the calculation without the QCSE.

(fully p_x- and p_y-like) is split from Γ_7 spin-orbit split-off hole by 90 meV. The potential depth of the Γ^9 Bloch state is 258 meV and the confinement energy is 97 meV. The level is deeply confined and its corresponding envelope function indicates that it is robustly confined in the quantum well.

The next question is to propose a physical mechanism that enables us to interpret the 70 meV activation energy.

To do so, we have made a variational computation of the exciton binding energy following the approach of Refs. [43–45]. As indicated in Fig. 6 (full line), we computed a value of the electron-hole long-range Coulomb interaction at 77 meV for 2 nm thin $Ga_{0.2}Al_{0.8}N$ quantum well confining layers embedded into AlN barrier layers. The trend for an unrealistic situation in the absence of internal electric fields is also represented using a dashed line in Fig. 6. It has been added to illustrate the reduction of the long-range electron-hole Coulomb interaction for well widths larger than 5 nm in $Ga_{0.2}Al_{0.8}N$-AlN due to the quantum confined Stark effect (QCSE).

V. CONCLUSION

In conclusion, the performance of short-wavelength emitting $Ga_{0.2}Al_{0.8}N$ QWs (i.e., at 215 nm), as measured at low photoexcitation density, is thermally limited at high temperatures by the thermal dissociation of the confined exciton (activation energy of 70 meV) and by the thermal escape of both the electron and spin-orbit split-off hole from the active region (activation energy of 130 meV). The dissociation of the exciton pair reduces the intensity, but one must not forget that some of the carriers thus released are fully available to recombine with oppositely charged carriers already present in the crystal [the AlN template is, as is well known, heavily *n*-type doped, so the population of the minority carriers the split-off holes is an important quantity to have in mind]. This complementary recombination can also be radiative in nature and thus it can produce photoluminescence whose intensity is governed by the population of dissociated excitons (here the population of split-off holes). Consequently, the story does not end with the dissociation of the exciton through the disappearance of all the electrons and holes associated with these Coulombic excitations. The series of samples we grew for the purpose of the study presented here is not adapted for allowing to study this phenomenon: We studied the effect of annealing and dislocation densities in the AlN beneath the growth template. However, this paves the way to complementary investigations. An important

parameter to control, in the case of heteroepitaxy on sapphire substrates, is the thickness of the predeposited AlN growth template layer, in order to initiate the growth process on surfaces with the lowest possible dislocation density, thereby limiting all defect-related nonradiative recombination mechanisms. The thermal ionization of excitons at high temperatures is intrinsic in nature, activated by an energy similar to the exciton binding energy. With rising temperature, the increased mobility of excitons promotes their diffusion toward dislocations and their dissociation into electron and hole pairs. This results in their thermal escape out from the active region. This enhances nonradiative recombination and limits the temperature dependence of the PL. An alternative potential option to partially mitigate these phenomena could be the growth of MQWs under nonpolar or semipolar orientations on sapphire. The ultimate solution could be the growth on high-quality AlN substrates.

ACKNOWLEDGMENTS

A.I. acknowledges the support of the French National Research Agency through ANR Project No. ANR-22-CE51-0035 "DOPALGAN" for the funding of her Ph.D. grant. The authors acknowledge the support by the French National Research Agency through ANR Project GANEX (ANR-11-LABX-0014). GANEX belongs to the publicly funded "Investissements d'Avenir" program managed by the French ANR agency.

DATA AVAILABILITY

There are no publicly available research data or software supporting this manuscript. Requests for further information or data should be sent to the authors.

[1] https://unfccc.int/process-and-meetings/the-kyoto-protocol.

[2] Y. Cheng, H. Chen, L. A. Sánchez Basurto, V. V. Protasenko, S. Bharadwaj, M. Islam, and C. I. Moraru, Inactivation of *Listeria* and *E. coli* by deep-UV LED: Effect of substrate conditions on inactivation kinetics, Sci. Rep. **10**, 3411 (2020).

[3] V. K. Sharma and H. V. Demir, Bright future of deep-ultraviolet photonics: Emerging UVC chip-scale light-source technology platforms, benchmarking, challenges, and outlook for UV disinfection, ACS Photon. **9**, 1513 (2022).

[4] P. Zwicker, J. Schleusener, S. B. Lohan, L. Busch, C. Sicher, S. Einfeldt, M. Kneissl, A. A. Kühl, C. M. Keck, C. Witzel, A. Kramer, and M. C. Meinke, Application of 233 nm far-UVC LEDs for eradication of MRSA and MSSA and risk assessment on skin models, Sci. Rep. **12**, 2587 (2022).

[5] G. Matafonova and V. Batoev, Recent advances in application of UV light-emitting diodes for degrading organic pollutants in water through advanced oxidation processes: A review, Water Res. **132**, 177 (2018).

[6] X. Li, M. Cai, L. Wang, F. Niu, D. Yang, and G. Zhang, Evaluation survey of microbial disinfection methods in UV-LED water treatment systems, Sci. Total Environ. **659**, 1415 (2019).

[7] H. Inagaki, A. Saito, H. Sugiyama, T. Okabayashi, and S. Fujimoto, Rapid inactivation of SARS-CoV-2 with deep-UV LED irradiation, Emerg. Microbes Infect. **9**, 1744 (2020).

[8] D. K. Kim and D. H. Kang, UVC LED irradiation effectively inactivates aerosolized viruses, bacteria, and fungi in a chamber-type air disinfection system, Appl. Environ. Microb. **84**, e00944 (2018).

[9] C. J. Zollner, S. P. DenBaars, J. S. Speck, and S. Nakamura, Germicidal ultraviolet LEDs: A review of applications and semiconductor technologies, Semicond. Sci. Technol. **36**, 123001 (2021).

[10] M. Ajmal, A. Nijabat, I. Sajjad, S. Z. Haider, W. Bedale, J.-H. Yu, M. A. Shah, C. Ukozehasi, M. A. Alwaili, and A. Elkelish, Evaluation of basil essential oils for antifungal and anti-aflatoxigenic activity against *Aspergillus flavus*, Sci. Rep. **15**, 19972 (2025).

[11] C. Hong, F. Zhao, S.-B. Song, S. Yoon, S.-J. Jeon, M. A. Khan, Y. Tao, D.-H. Yang, W. Lee, J. Kim, *et al.*, Highly efficient, deep-ultraviolet luminescence in hBN moiré quantum wells, Science **391**, eaeb2095 (2026).

[12] B. Gil and G. Cassabois, Strong light emission with a twist, Science **391**, 1204 (2026).
[13] T. Kirihara, M. A. Khan, M. N. Sharif, Y. Nagata, A. Yasin, H. Yaguchi, and H. Hirayama, 225 nm far-UVC LEDs enabled directly on c-sapphire by tailored AlN molar fraction in n-AlGaN layers, J. Appl. Phys. **138**, 174501 (2025).
[14] T.-Y. Seong, J. Han, H. Amano, and H. Morkoç, *Topics in Applied Physics* (Springer, Heidelberg, 2013), Vol. 126.
[15] T. D. Moustakas and R. Paiella, Optoelectronic device physics and technology of nitride semiconductors from the UV to the terahertz, Rep. Prog. Phys. **80**, 106501 (2017).
[16] K. B. Nam, M. L. Nakarmi, J. Li, J. Y. Lin, and H. X. Jiang, Mg acceptor level in AlN probed by deep ultraviolet photoluminescence, Appl. Phys. Lett. **83**, 878 (2003).
[17] J. L. Lyons and C. G. Van de Walle, Computationally predicted energies and properties of defects in GaN, npj Comput. Mater. **3**, 12 (2017).
[18] A. Walsh and A. Zunger, Instilling defect tolerance in new compounds, Nat. Mater. **16**, 964 (2017).
[19] K. B. Nam, J. Li, M. L. Nakarmi, J. Y. Lin, and H. X. Jiang, Unique optical properties of AlGaN alloys and related ultraviolet emitters, Appl. Phys. Lett. **84**, 5264 (2004).
[20] R. G. Banal, M. Funato, and Y. Kawakami, Optical anisotropy in [0001]-oriented $Al_xGa_{1-x}N$/AlN quantum wells ($x > 0.69$), Phys. Rev. B **79**, 121308(R) (2009).
[21] M. Kneissl, T.-Y. Seong, J. Han, and H. Amano, The emergence and prospects of deep-ultraviolet light-emitting diode technologies, Nat. Photon. **13**, 233 (2019).
[22] A. Ibanez, N. Nikitskiy, A. Zaiter, P. Valvin, W. Desrat, T. Cohen, M. Ajmal Khan, G. Cassabois, H. Hirayama, P. Genevet, J. Brault, and B. Gil, Excitons in (Al,Ga)N quantum dots and quantum wells grown on (0001)-oriented AlN templates: Emission diagrams and valence band mixings, J. Appl. Phys. **134**, 193103 (2023).
[23] A. Ibanez, M. Leroux, N. Nikitskiy, W. Desrat, M. Moret, P. Valvin, G. Cassabois, J. Brault, B. Gil, F. Chugenji, K. Taiga, M. A. Khan, and H. Hirayama, The influence of alloy disorder effects on the anisotropy of emission diagrams in (Al,Ga)N quantum wells embedded into AlN barriers, Phys. Status Solidi B **261**, 2400215 (2024) and references therein.
[24] F. Bernardini, V. Fiorentini, and D. Vanderbilt, Spontaneous polarization and piezoelectric constants of III-V nitrides, Phys. Rev. B **56**, R10024 (1997).
[25] T. Takeuchi, H. Takeuchi, S. Sota, H. Sakai, H. A. Hiroshi Amano, and I. A. Isamu Akasaki, Optical properties of strained AlGaN and GaInN on GaN, Jpn. J. Appl. Phys. **36**, L177 (1997).
[26] T. Takeuchi, C. Wetzel, S. Yamaguchi, H. Sakai, H. Amano, I. Akasaki, Y. Kaneko, S. Nakagawa, Y. Yamaoka, and N. Yamada, Determination of piezoelectric fields in strained GaInN quantum wells using the quantum-confined Stark effect, Appl. Phys. Lett. **73**, 1691 (1998).
[27] S. F. Chichibu, A. C. Abare, M. S. Minsky, S. Keller, S. B. Fleischer, J. E. Bowers, E. Hu, U. K. Mishra, L. A. Coldren, S. P. Denbaars, and T. Sota, Effective band gap inhomogeneity and piezoelectric field in InGaN/GaN multiquantum well structures, Appl. Phys. Lett. **73**, 2006 (1998).
[28] J. S. Im, H. Kollmer, J. Off, A. Sohmer, F. Scholz, and A. Angleiter, Reduction of oscillator strength due to piezoelectric fields in GaN/$Al_xGa_{1-x}N$ quantum wells, Phys. Rev. B **57**, R9435 (1998).
[29] M. Leroux, N. Grandjean, M. Laügt, J. Massies, B. Gil, P. Lefebvre, and P. Bigenwald, Quantum confined Stark effect due to built-in internal polarization fields in (Al,Ga)N/GaN quantum wells, Phys. Rev. B **58**, R13371 (1998).
[30] M. Leroux, N. Grandjean, J. Massies, B. Gil, P. Lefebvre, and P. Bigenwald, Barrier-width dependence of group-III nitrides quantum-well transition energies, Phys. Rev. B **60**, 1496 (1999).
[31] A. E. Romanov, T. J. Baker, S. Nakamura, and J. S. Speck, Strain-induced polarization in wurtzite III-nitride semipolar layers, J. Appl. Phys. **100**, 023522 (2006).
[32] https://www.sino-gan.com.
[33] S. Matta, J. Brault, M. Korytov, T. Q. Phuong Vuong, C. Chaix, M. Al Khalfioui, P. Vennéguès, J. Massies, and B. Gil, Properties of AlN layers grown on c-sapphire substrate using ammonia assisted MBE, J. Cryst. Growth **499**, 40 (2018).

[34] S. Hagedorn, S. Walde, A. Knauer, N. Susilo, D. Pacak, L. Cancellara, C. Netzel, A. Mogilatenko, C. Hartmann, T. Wernicke, M. Kneissl, and M. Weyers, Status and prospects of AlN templates on sapphire for ultraviolet light-emitting diodes, Phys. Status Solidi A **217**, 1901022 (2020).

[35] M. Nemoz, R. Dagher, S. Matta, A. Michon, P. Vennéguès, and J. Brault, Dislocation densities reduction in MBE-grown AlN thin films by high-temperature annealing, J. Cryst. Growth **461**, 10 (2017).

[36] A. Ibanez, P. Ščajev, M. Ajmal Khan, K. Fujimoto, S. Mitra, P. Valvin, G. Cassabois, M. Leroux, J. Brault, H. Hirayama, and B. Gil, Extrinsic and intrinsic nonradiative recombination channels in deep ultraviolet ($\lambda < 230$ nm) light emitting heterostructures made of group III element nitrides, J. Appl. Phys. **139**, 085702 (2026).

[37] L. Cancellara, T. Markurt, T. Schulz, M. Albrecht, S. Hagedorn, S. Walde, M. Weyers, S. Washiyama, R. Collazo, and Z. Sitar, Role of oxygen diffusion in the dislocation reduction of epitaxial AlN on sapphire during high-temperature annealing, J. Appl. Phys. **130**, 203101 (2021).

[38] S. F. Chichibu, K. Kikuchi, B. Moody, S. Mita, R. Collazo, Z. Sitar, Y. Kumagai, S. Ishibashi, A. Uedono, and K. Shima, Roles of Al-vacancy complexes on the luminescence spectra of low dislocation density Si-doped AlN grown by halide vapor phase epitaxy, Appl. Phys. Lett. **126**, 111905 (2025).

[39] B. E. Gaddy, Z. Bryan, I. Bryan, J. Xie, R. Dalmau, B. Moody, Y. Kumagai, T. Nagashima, Y. Kubota, T. Kinoshita, A. Koukitu, R. Kirste, Z. Sitar, R. Collazo, and D. L. Irving, The role of the carbon-silicon complex in eliminating deep ultraviolet absorption in AlN, Appl. Phys. Lett. **104**, 202106 (2014).

[40] D. Rosales, T. Bretagnon, B. Gil, A. Kahouli, J. Brault, B. Damilano, J. Massies, M. V. Durnev, and A. V. Kavokin, Excitons in nitride heterostructures: From zero- to one-dimensional behavior, Phys. Rev. B **88**, 125437 (2013).

[41] A. David and N. Grandjean, The physics of GaN-based light-emitting diodes, Nat. Rev. Phys. **8**, 477 (2026).

[42] A. David, Optical properties of (In,Ga)N quantum wells: Accurately modeling the effects of disorder, Phys. Rev. Appl. **26**, 014034 (2026).

[43] G. Bastard, E. E. Mendez, L. L. Chang, and L. Esaki, Exciton binding energy in quantum wells, Phys. Rev. B **26**, 1974 (1982).

[44] G. Bastard, E. E. Mendez, L. L. Chang, and L. Esaki, Variational calculations on a quantum well in an electric field, Phys. Rev. B **28**, 3241 (1983).

[45] P. Bigenwald, P. Lefebvre, T. Bretagnon, and B. Gil, Confined excitons in GaN-AlGaN quantum wells, Phys. Status Solidi B **216**, 371 (1999).